Magnetite-latex nanoparticle motion during capillary uptake in thin, porous layers studied with UFI-NMR

Colloids and Surfaces A: Physicochemical and Engineering Aspects 683 (2024) 133011

Contents lists available at ScienceDirect

Colloids and Surfaces A: Physicochemical and Engineering Aspects

journal homepage: www.elsevier.com/locate/colsurfa

Magnetite-latex nanoparticle motion during capillary uptake in thin, porous layers studied with UFI-NMR

R.J.K. Nicasy [a,1], A. Barquero [d], H.P. Huinink [a,*,1], S.J.F. Erich [a,b,1,2], O.C.G. Adan [a,b,1,2], N. Tomozeiu [c], H. Mansouri [c], J. Scheerder [e]

[a] Eindhoven University of Technology, Applied Physics Department, P.O. Box 513, Eindhoven 5600 MB, the Netherlands
[b] Organization of Applied Scientific Research, TNO, P.O. Box 49, Delft 2600 AA, the Netherlands
[c] Canon Production Printing, Venlo, the Netherlands
[d] POLYMAT, Department of Applied Chemistry, University of the Basque Country UPV/EHU, Avenida de Tolosa, 72, Donostia-San Sebastian 20018, Spain
[e] Covestro (Netherlands) B.V., Sluisweg 12, 5145 PE Waalwijk, the Netherlands

GRAPHICAL ABSTRACT

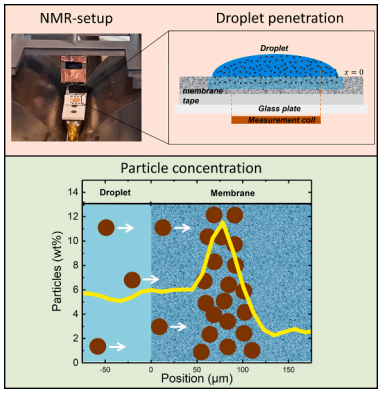

ARTICLE INFO

Keywords:
Iron-oxide nanoparticles
Membranes
NMR imaging
Capillarity
SEM
Particle adsorption

ABSTRACT

The transport of nanoparticles in porous media has received growing attention in the last decades due to environmental concerns in, for example, the printing industry, filtration, and transport of pollutants. Experimental studies on the imbibition of particle dispersions in porous media with sufficiently high spatial and temporal resolution are still challenging. This study shows how Ultra-Fast Imaging (UFI) NMR is an ideal tool for studying Fe_3O_4-latex particles penetration with a temporal resolution of 15 ms and spatial resolution of 18 μm. In the first part, it is shown that a calibration curve between the UFI-NMR signal intensity and the particle concentration exists. In the second part, UFI-NMR is used to study the penetration of a particles inside a thin nylon membrane during capillary uptake, which revealed liquid-particle front splitting and an inhomogeneous buildup of the particle concentration. Both the liquid-particle front splitting and inhomogeneous build up could be

* Correspondence to: Eindhoven Institute of Renewable Energy Systems, Eindhoven University of Technology, PO Box 513, Eindhoven 5600 MB, the Netherlands.
E-mail address: h.p.huinink@tue.nl (H.P. Huinink).
[1] Transport in Permeable Media group, Department of Applied Physics, Eindhoven University of Technology, PO Box 513, Eindhoven 5600 MB, the Netherlands.
[2] TNO Materials Solution, High Tech Campus 25 Eindhoven, Netherlands.

https://doi.org/10.1016/j.colsurfa.2023.133011
Received 5 September 2023; Received in revised form 30 November 2023; Accepted 15 December 2023
Available online 18 December 2023

verified by Scanning Electron Microscopy. Our method allows to determine particle concentration profiles during capillary uptake within thin, porous media. Therefore, the technique can be easily extended to study particle penetrations in a wide variety of systems such thin interfaces, biomaterials, films, and filter media.

1. Introduction

The transport of nanoparticles and colloids within porous media has received growing attention in the last decades in view of a wide variety of applications ranging from filtration processes (bacteria [1], viruses [2], colloids [3] and drinking water [4,5]), transport of pollutants in soil [6–8], transport of biomarkers in wearable electronics [9–11] and ink penetration [12–14]. In most applications, particle transport is directly linked to performance or quality: for example the print quality in paper [15,16] or filtration efficiency of a filter [17,18]. A better understanding of liquid and particle transport through porous media is of great importance for improving the performance of these applications.

Important parameters are the particle penetration depth, the deposition rate and the separation of particle sizes. A detailed review of the transport of nanoparticles in porous media is given by Boccardo et al. [19]. One way to study these processes is through theoretical models that try to simulate particle transport [20,21]. Such models showed that the particle retention was greatly dependent on porosity, flow rate of the carrying fluid and matrix-particle interaction [21]. However, because porosity and permeability depend on the particle deposition within the porous media, the application of these models is very difficult.

Besides theoretical models, there are many experimental methods for studying transport of particles in porous media. Most of the experimental studies measure particle retention in columns filled with porous materials [6–8,22]. In the experiment, a particle suspension is injected and pushed through a porous media (column). Data is gathered by analyzing the residue from the column with a breakthrough curve, which represent the particle concentration in the residue as a function of input liquid volume. These studies allow to determine the deposition rate of the particles within the porous media and showed that the particle recovery rate increased by increasing the fluid velocity [7]. Although experimental methods for measuring nanoparticle dynamics are quite abundant for larger time (>1 min) and length scales (> 1 mm), experimental studies on fast penetration (< 100 ms) in thin-porous media (< 100 μm) are still challenging. Some attempts have been made to measure the particle penetration in thin porous media using microscopic techniques, such as scanning electron microscopy (SEM) [23], focused ion beam (FIB) [12] or confocal laser scanning microscopy [24]. These techniques can achieve high-spatial resolution, but require a cross-section of the sample resulting in irreversible damage. Using these techniques, only post-mortem images can be made of the particle distributions. These techniques can provide good results on the final distributions, but will not provide information during transport.

Another type of experimental techniques that can cope with the fast measuring time are ultra-sonic liquid penetration (ULP) [25,26], drop adsorption (DA) or scanning automatic absorptometer (ASA) [27] which provide information on timescales as low as 10 ms. However, these techniques are only able to measure the liquid uptake within the porous medium and therefore only information about the effect of particles on the liquid uptake process. With these techniques, no particle distributions can be determined and only limited amount of information can be gained about the particle-matrix interaction. Therefore, a technique that is able to measure particle distributions during transport at sufficient time and length scales would be of great importance.

In a previous study, Ultra-Fast Imaging (UFI) NMR proved an ideal tool to study capillary uptake in thin-porous membranes with a high spatial (18 μm) and temporal (10 ms) resolution [28-30]. Until now, only the capillary uptake of water-glycerol mixtures was studied, and no studies were performed on the uptake of particle dispersions. The NMR ability to image particles and colloids was already shown in a wide variety of studies [31,32]. However, these studies are unable to cope with the high temporal and spatial resolution required to measure capillary uptake within thin, porous media. In this study, it will be shown how the UFI method is able to study the transport of iron oxide nanoparticles during capillary uptake within thin nylon membrane filters. The technique can be easily extended and used to study a wide variety of applications that include penetration of particles and colloids within thin, porous media.

In this study, it is first shown how the iron oxide within the latex particles enables the quantification of the latex particle concentration by the UFI-NMR method. Secondly, it is demonstrated how the UFI-NMR method is able to measure the position of latex particles during capillary uptake with a temporal resolution of 25 ms and a spatial resolution of 18 μm. Furthermore, it is shown how particle concentration profiles within the nylon membranes can be determined. Finally, the UFI-NMR results are compared to scanning electron microscopy images.

2. Materials and methods

2.1. Styrene- Fe_3O_4 hybrid particles

First, iron oxide nanoparticles were synthetized as described by Lu et al. [33]. In a 2 L jacketed glass reactor, iron (III) chloride hexahydrate ($FeCl_3$·6 H_2O, 27.02 g) and iron (II) chloride tetrahydrate ($FeCl_2$·4 H_2O, 9.90 g) were dissolved in water (650 g) at 25.0 °C. Oleic acid (10 g) was dissolved in acetone (60 ml) and added to the reactor and mixed for 30 min. NH_4OH (25 wt% solution in water, 75 ml) was added dropwise in 10–15 min under N_2 atmosphere to the reactor and mixed for 1 h. After that the temperature was increased to 85.0 °C for 1 h. The reaction mixture was cooled down to 70.0 °C and HCl (2 N solution) was added until pH 2 was obtained. Under the acid pH the nanoparticles coagulated. The nanoparticles were washed with deionized water until the pH of the washing water was 7 and were dried in an oven (at 65.0 °C) for 48 h.

In a next step, polystyrene-Fe_3O_4 hybrid nanoparticle latexes were synthetized by mini-emulsion polymerization, using 100 ml bottles submerged in a water tank and tumbled end over end at 70.0 °C for 24 h. The mini-emulsion was obtained by sonicating the mixture of the water and organic phases in a Branson Digital Sonifier for 20 min at 80% amplitude and a 0.8 s on and 0.2 s off cycle in an ice bath under magnetic stirring. The compositions of the organic and water phases for each polymerization are summarized in Table 1. Styrene (S), which is the main monomer, is converted to polystyrene in the final latex. methacrylic acid (MAA) is used as comonomer and sodium dodecyl sulfate (SDS) as surfactant, azobisisobutyronitrile (AIBN) is the initiator and hexadecane (HD) is used as costabilizer to keep the stability of the mini-emulsion during the polymerization process. Three latexes of 30% S.C. were obtained with Fe_3O_4 concentrations from 0.5 to 5.0 wt% (based on total dispersed phase).

2.2. Liquid solutions

In this study, liquid solutions are made by mixing demineralized water (type I), glycerol, Clariscan and the Fe_3O_4-latex particles, see Table 1. Solutions were coded by GxPyFz where x gives the wt% of glycerol, y the wt% of particles and z the wt% of Fe_3O_4 within the particles. Clariscan ($C_{16}H_{25}GdN_4O_{87}$) is a gadolinium based contrast agent commonly used in medical MRI [34]. It is provided in a water like solution with a concentration of 279.3 mg/ml (0.5 M). The Clariscan solution has a pH between 6.5 and 8, a density of 1.349 g/ml and a

viscosity of 3.0 mPa.s at room temperature [35]. The goal of the Clariscan is to change the T_1-relaxation time and allow fast imaging by UFI. The concentration of Clariscan was determined based on an earlier described method [29]. The glycerol (> 99.0% purity) has a density of 1.26 g/ml and is used to tune the viscosity of the liquid solutions.

For calibration of the signal intensity, four different glycerol contents were used (0 wt%, 25 wt%, 50 wt% and 70 wt%). The actual penetration experiments were only done with mixtures containing 70 wt% (G70) of glycerol and use the particles with 0.5 wt% of iron oxide (F0.5). To study the effect of particle concentration, the particle concentration was varied between 0 (P0) and 8 wt% (P8). Experiments with lower viscosities can be performed but would lower the signal-to-noise ratio. When taking the spatial resolution (14.5 μm) and the measurement time (11.6 ms), an estimate about the maximum penetration speed can be given. When the distance that the liquid moves within the measurement time exceeds the spatial resolution, the decrease in signal-to-noise ratio becomes problematic. Therefore, the penetration speed limit for our experiments is 1.25 μm/s.

2.3. Membranes

For the penetration experiments, Whatman nylon-6,6 membranes (from VWR) are used with a typical pore radius of 0.2 μm (nylon-membrane I) and 0.45 μm (nylon-membrane II). The membranes have a thickness of 170 μm and a porosity of 65%.

2.4. NMR

In a previous study, it was shown that the UFINMR method was able to measure the absorption of liquids in thin, porous media with a time resolution of 10 ms [29,30]. In this study, it will be shown that the same technique can be used to study the transport of Fe_3O_4 latex particles. This section will start by a discussion of the pulse sequences, followed by a discussion of the signal characterization. Thereafter, the signal characterization will be used to discuss the NMR-signal profiles for four typical imbibition cases: 1) a pure liquid without particles, 2) particle dispersion that during imbibition remains homogeneously mixed, 3) a particle dispersion with particles penetrating slower than the liquid phase, and 4) a particle dispersion with particles not entering the porous material. Finally, the experimental procedure and NMR settings will be described.

2.4.1. Pulse sequences

2.4.1.1. Saturation recovery (T_1). To characterize the effect of the Fe_3O_4-latex particles on the T_1 relaxation time, measurements are performed with a saturation recovery sequence: $[\alpha_y^\circ - \tau_1]_m - \tau_2 - 90_x^\circ - \tau - 90_y^\circ -$ echo. Here, m denotes the amount of saturation pulses and α represents the flip angle [36,37]. To increase the signal-to-noise ratio, multiple measurements are performed and averaged. The time between two measurements (pulse sequences) is given by the repetition time ($t_r(s)$).

2.4.1.2. Ostroff-Waugh (T_2). To characterize the effect of the Fe_3O_4 latex particles on the T_2 relaxation time, measurements of the T_2-relaxation times are performed by an Ostroff- Waugh (OW) [37,38] sequence given by $(90_x^\circ - \tau - [90_y^\circ - \tau - \text{echo} - \tau]_n)$, where n denotes the amount of echoes measured, α represents the flip angle and $2\tau = t_e(s)$ is the echo time. Similar to the saturation recovery sequence, the signal-to-noise will be increased by performing multiple measurements, where the time between two measurements (pulse sequences) is given by the repetition time ($t_r(s)$).

2.4.1.3. UFI (proton density). To measure the proton density profiles during penetration, the UFI method was used. UFI can measure proton densities with a spatial resolution of 18 μm and temporal resolution of 10 ms. To achieve these resolutions, the solutions T_1-relaxation time is decreased by the addition of a contrast agent (Clariscan).and different echoes are summed to have a high enough signal to noise ratio in a reasonable time period. The pulse sequence is given by $90_x^\circ - \tau - [90_y^\circ - \tau - (\text{echo}) - \tau - 90_{-y}^\circ - \tau - (-\text{echo}) - \tau]_N$, where $N$is the number of repetitions within one measurement. The final signal intensity is built up by a summation of all $2N$measured echoes. A detailed description of this UFI method can be found in [29].

2.4.2. NMR signal calibration

Because our NMR equipment is set to measure hydrogen nuclei, the signal originates either from hydrogen nuclei of the liquid solution or from the latex particles. However, because UFI is a T_2 weighted signal and the T_2-time of the polystyrene within the latex particles was as low as 100 μs, the polystyrene will not contribute to the signal intensity measured by UFI. Therefore, the only signal intensity that is measured is that of the liquid solution. The Fe_3O_4 within the latex particles will decrease the T_2-relaxation time of the surrounding liquid, which allows for the detection of the particles. Therefore, this section focuses on the effect of the particles on the NMR-signal of the liquid, with the goal to establish a calibration curve to determine the particle concentration. The signal intensity measured by UFI was determined in an earlier study (Eq. 4 of [29]) and is given by:

$$S = \rho \sum_{n=1}^{2N} \exp\left(-n\frac{t_e}{T_2}\right), \tag{1}$$

where ρ stands for the hydrogen density and $2N$is the number of echoes that are used for determining the signal profile. Due to the addition of Clariscan and its effect on the T_1-time, the following condition is always satisfied: $t_r/T_1 \ll 1$. Therefore, the $(1 - e^{-t_r/T_1})$ factor can be neglected within the UFI signal intensity.

Table 1
Composition of the latex particles in grams. The different components are: Fe_3O_4, styrene as the main monomer, Methacrylic acid (MAA) as comonomer, hexadecane (HD) as costabilizer, Azobisisobutyronitrile (AIBN) as initiator and sodium dodecyl sulfate (SDS) as surfactant.

	Organic phase						Water phase	
Latex	Fe_3O_4 (%)	Styrene (g)	Fe_3O_4 (g)	MAA (g)	HD (g)	AIBN (g)	Water (g)	SDS (g)
E	7.5	99.4	8.063	3.225	8.600	2.150	250.84	2.72
F	5	102.1	5.375	3.225	8.600	2.150	250.84	2.69
G	2.5	104.8	2.688	3.225	8.600	2.150	250.84	2.69
H	0.5	107.0	0.538	3.225	8.600	2.150	250.84	2.69
I	0.1	107.5	0.108	3.225	8.600	2.150	250.84	2.72

When the Fe_3O_4-latex particles are introduced to the liquid solution, the Fe_3O_4 will influence the signal of the surrounding nuclei via the T_2 according to [39,40],

$$\frac{1}{T_2} = \frac{1}{T_{2bulk}} + R_2 C \tag{2}$$

with R_2(ms.wt%$^{-1}$) being the relaxivity of the Fe_3O_4-latex particles and C (wt%) the particle concentration. Another effect that should be considered when introducing latex particles, is the replacement of water by latex particles. As explained before, hydrogen nuclei of the latex particles are invisible for UFI. Therefore, signal will be lost when replacing water molecules by latex particles. Therefore, ρ is replaced by $\rho_{max}(1 - aC)$, where ρ_{max} is the density of visible hydrogen nuclei in a pure liquid. The variable a (wt%$^{-1}$), called the density change factor, is a constant that represents the decrease in liquid hydrogen nuclei per wt% of latex particles introduced in the suspension. When introducing both relations in Eq. 1, the signal intensity in a UFI experiment becomes:

$$S(C) = \rho_{max}\left(1 - aC\right)\sum_{n=1}^{2N}\exp\left(-nt_e\left[\frac{1}{T_{2bulk}} + R_2 C\right]\right). \tag{3}$$

If the signal intensity is taken relative to the signal of a solution containing no particles $S = \rho_{max}\sum_{n=1}^{2N}\exp(-nt_e/T_{2bulk})$. The relative signal becomes:

$$S'(C) = \left(1 - aC\right)\sum_{n=1}^{2N}\exp(-nt_e R_2 C), \tag{4}$$

where it can be seen that $S'(0) = 1$. Here, it is assumed that the $T_{2bulk}$of the solution does not change by introducing latex particles. Once again, this underlines adding particles decreases the measured signal intensity by 2 effects: by decreasing the amount of water molecules and lowering the T_2 - relaxation time.

In Fig. 1, the relative signal intensity S' is plotted for different concentrations of particles. The relaxation values and a are set to 0.095 ms^{-1}wt%$^{-1}$ and 0.016 wt%$^{-1}$, respectively. These values correspond to a mixture containing 70 wt% glycerol and particles with 0.5 wt % of iron oxide and are determined in section 3.1.2. For the echo time, 50 μs is used. The signal decrease due to a lowering of the hydrogen atoms is drawn in black-dashed while the T_2-effect is drawn in orange-dashed. The total calibration curve is a combination of both effects and is drawn in blue-solid. The resulting calibration curve allows to extract the particle concentration from the signal.

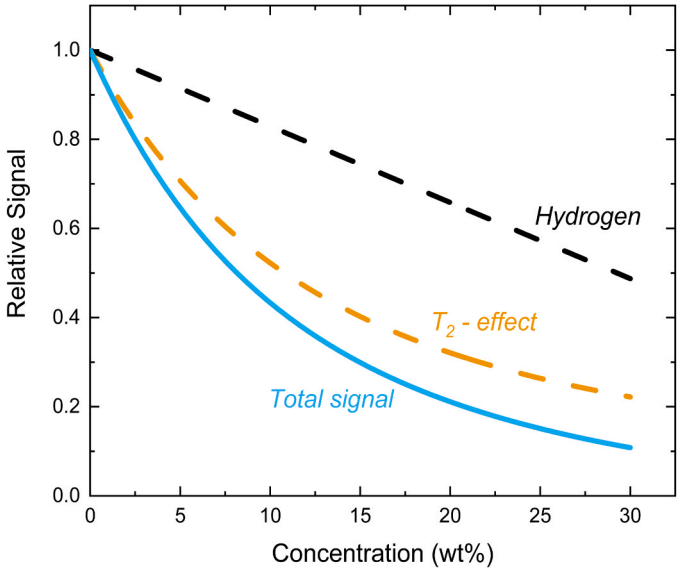

Fig. 1. UFI NMR signal as a function of the particle concentration (blue). Shown in orange and black dashed lines are the contributions coming from the decrease in -relaxation and the decrease of hydrogen atoms respectively.

2.4.3. Typical NMR signal profiles for different cases

When a particle dispersion penetrates in a thin, porous media, three typical situations can occur. Firstly, the particles and liquid move together as a homogeneous mixture and the particle and liquid front coincide. Secondly, the particles move slower than the liquid leading to a splitting of the particle and liquid front. Thirdly, the particles cannot enter the porous membrane, and a particle layers forms on top of the membrane. Because the measured NMR-signal is a function of the particle concentration (Eq. 4), all the above-mentioned cases will have their typical NMR-signal profiles. A better understanding of these NMR-signal profiles will help in understanding the measured profiles during uptake experiments. Therefore, a more theoretical discussion about the NMR-profiles will be given in this section.

In the top of Fig. 2, the different situations are schematically drawn. The figures represent the penetration of liquid (blue) and particles (orange dots) in the nylon membranes (gray). The figures show 50 μm of the droplet on the left followed by the nylon membrane where the interface is marked with a green dashed line. The liquid and particles move from left to right and their corresponding fronts are marked with respectively a black and orange dashed line. The middle figures show the corresponding wt% of liquid (blue-dashed) and particles (red-solid). The lowest figures represent the corresponding NMR-profiles. The NMR-profiles are simulated using MATLAB based on the NMR-system specifications (echo time of 50 μs and a sample rate of 5 MHz), which results in a theoretical spatial resolution of 14.5 μm. To calculate the signal intensities, the calibration curve for a mixture containing 70 wt% glycerol and particles with 0.5 wt% of iron oxide is used (blue-solid line in Fig. 1). The start concentration of particles used in this discussion is 5 wt%, which corresponds to a relative value of 0.65. In the following subsections, we will discuss these potential situations in more detail.

2.4.3.1. A pure liquid without particles (A). In Fig. 2A, the reference situation, where only liquid penetrates the nylon membrane is shown. The liquid content is always 100 wt% but drops to 0 after the liquid front. The corresponding NMR-profile shows first the droplet region with a signal intensity of 1, meaning a fully saturated region with only liquid. Within the membrane, the signal intensity of a fully saturated region drops to 0.65 as a consequence of the porosity (65%). Ahead of the liquid front ($x > 100$ μm), no liquid is found, which results in a signal intensity of zero. From the reference, it can be observed that the NMR-resolution will have a significant effect on the NMR-profiles, which can be observed in the gradual change in signal intensity at the droplet-membrane and liquid front interface. Experimental measurements of this situation can be found in earlier research, where the penetration of water-glycerol mixtures was measured within nylon- and PVDF-membranes [28,29].

2.4.3.2. Homogeneous movement of liquid and particles (B). In the second situation (Fig. 2B), the particles move together with the liquid and, therefore, the liquid front (black-dashed line) and particle front (orange-dashed line) coincide. In this particular case, the particle concentration was set to 5 wt%. As there is no blocking of particles, at the droplet-liquid interface, the particle concentration everywhere in the liquid phase is 5 wt% (Fig. 2B, middle). Because the particles are homogeneously distributed, their effect on the signal intensity will be the same at every position. Therefore, the profile is similar to the reference but lowered with a factor of 0.65 due to the presence of particles.

2.4.3.3. The particle front lags behind the liquid front (C). In the third case, a splitting between the particle front and liquid front occurs. In Fig. 2C top, the particles front has reached a depth of 50 μm (orange-dashed), while the liquid front has already reached 100 μm (black-

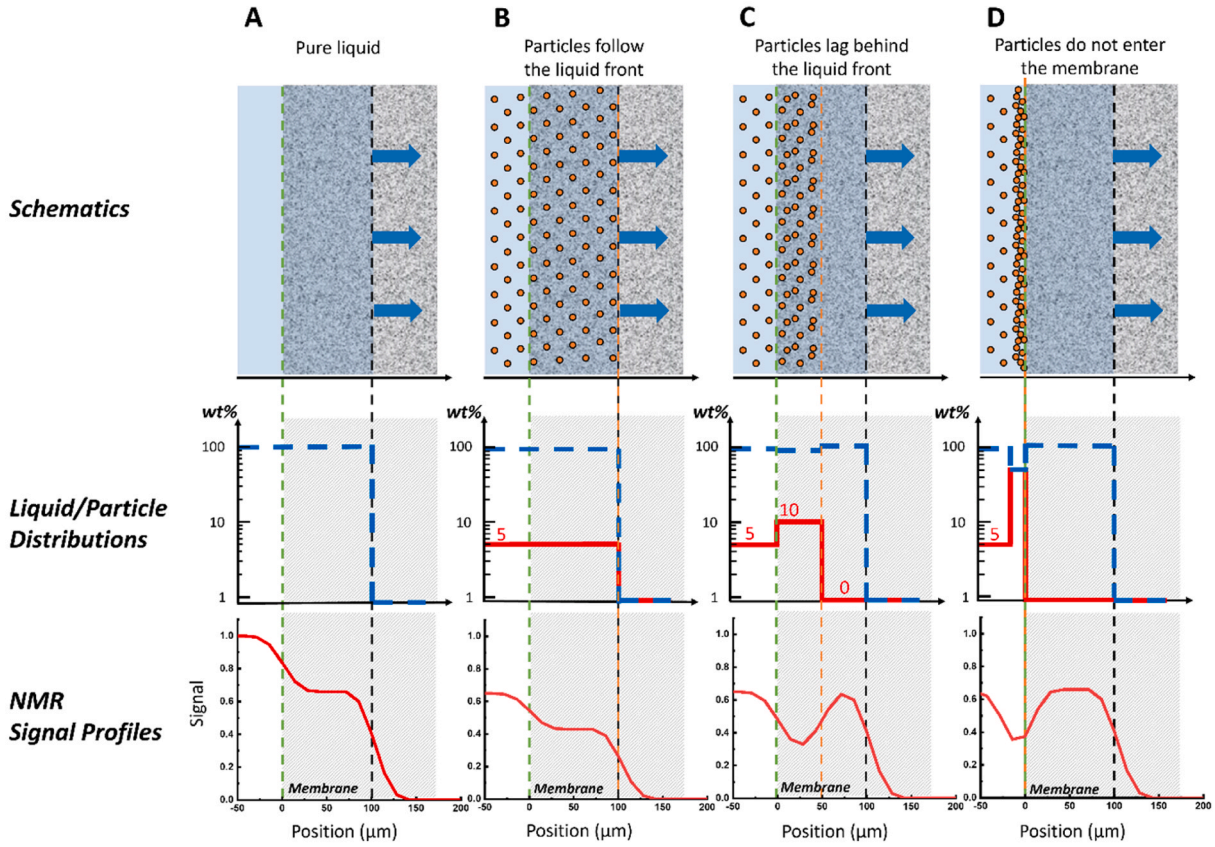

Fig. 2. Representation of four different archetypical situations that can occur during particle penetration. From left to right these four situations (top row), corresponding fluid and particle distributions (middle row) and resulting NMR signal profiles (bottom row) are shown. The four situations are A) pure liquid penetration, B) homogeneous movement of liquid and particles, C) splitting between particle and liquid front and D) particles cannot enter the porous media.

dashed line). Fig. 2C middle, shows the particle concentration throughout the sample starting with 5 wt% in the droplet, 10 wt% until 50 μm followed by a region with no particles. The increased particle concentration in the upper part of the membrane can be attributed to the slower movement of the particles, which results in a buildup of particles. From the calibration curve, we know that the signal will be higher in absence of particles, therefore the signal will start to increase again around 50 μm. The corresponding NMR-profile can be seen in the bottom of Fig. 2C, where a clear increase in signal intensity is found beyond 50 μm. When the separation between the particle and liquid front is larger than two times the resolution (29 μm), the signal intensity will increase back to its original intensity found within the reference. In this way, the NMR-profiles could be used to identify a splitting in particle- and liquid- front. The position of this particle front is situated at the position where the increase in signal intensity is at half maximum (the orange-dashed line).

2.4.3.4. Particle cannot enter the porous media (D). In the last situation, the particles do not enter the porous membrane, while the liquid penetrates (Fig. 2D). In this situation, the particles are clogged and stay at the droplet-membrane interface (green-dashed line), where they will create a dense particle layer. In this example, an arbitrary particle layer with thickness of 20 μm and a particle content of 50 wt% was chosen. Inside the medium only water can be found, which can be seen in the middle figure. The dense particle layer results in a decreased NMR-signal intensity on top of the membrane. Similar to the situation where particles lag behind the liquid front, the signal starts to increase to its original value within the membrane ($x > 0$ μm), because only liquid is present here. As the particle layer at the top is smaller than 2 times the resolution (29 μm), the signal at the droplet-membrane interface will not reach zero.

2.5. Experimental details and setup

The NMR setup used in this study is a GARField-NMR with a magnetic field of 1.46 T and a gradient of 40.3 T/m which is thoroughly described in earlier work [29]. The GARField NMR uses a Radio Frequency coil (measurement coil) to record the signal intensity. Fig. 3 shows a schematic representation of the droplet insert, light sensor, measurement coil and a typical sample during the penetration of a particle suspension. Next to the sample, the corresponding UFI signal profile is shown. In this example, the particle suspension penetrates the nylon membrane as described by Section 2.4.3.3 where the particle front $p(t)$(orange-dashed line) lags behind the liquid front $l(t)$(blue-dashed line).

An experiment starts by jetting a droplet (8–12 μL) on top of a nylon membrane, which triggers a light sensor that will start the UFI pulse sequence. The measurement area is located above the measurement coil and indicated with a black box. The corresponding UFI measurement is a 1D-profile of the situation within this black box.

The settings used for the UFI pulse sequence are $t_e = 50$μs, a window width of 40 μs, and $N = 16$. These settings result in a theoretical spatial resolution of 14.5 μm. The experimental resolution was determined to be 18 μm. The $t_r$was varied between 10 and 300 ms depending on the speed of the penetration experiment.

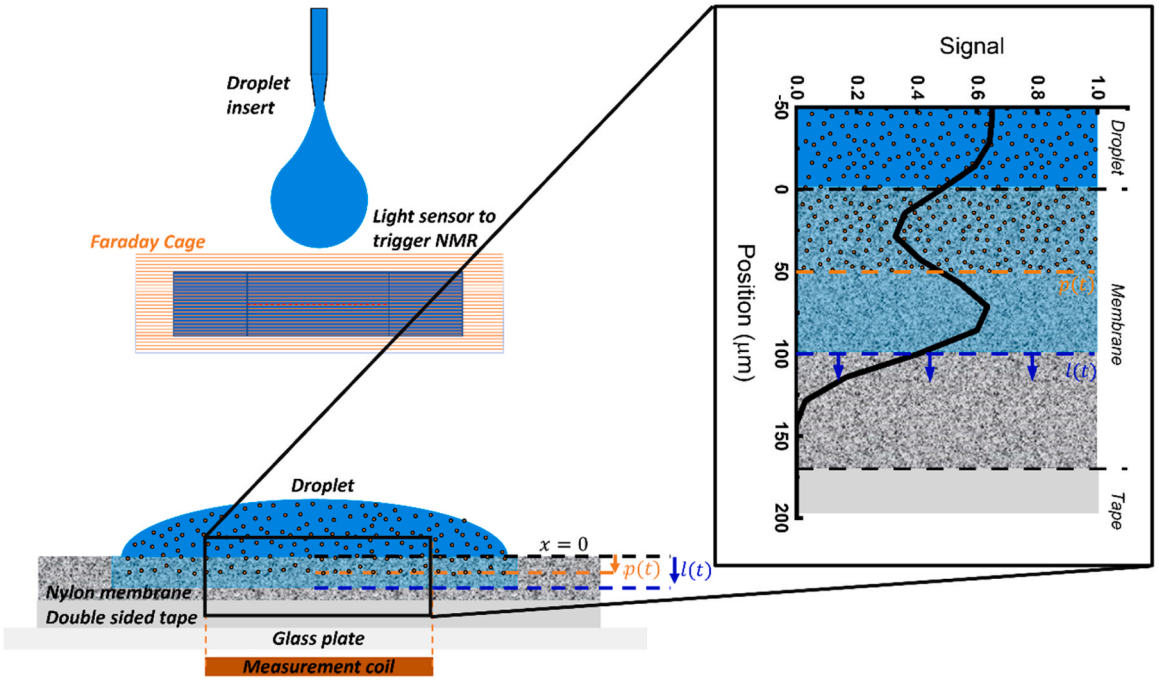

Fig. 3. Schematic picture of the measurement insert. Shown are the droplet insert, the light sensor to trigger the NMR, the sample with droplet and the RF coil to measure the signal. A signal profile that corresponds with the 3-dimensional situation is shown in the indent.

3. Results and discussion

3.1. Characterization of the particles

To characterize the particles, particle size distributions were measured for both the hybrid iron oxide latex particles and the iron oxide particles themselves. Additionally, STEM images of the hybrid iron oxide latex particles are provided which depict both the complete particles and individual iron oxide nanoparticles.

Fig. 4 shows the particle size distributions of the Fe_3O_4–polystyrene latex particles containing 0.5 wt% (black), 2.5 wt% (orange) and 5 wt% (blue) of Fe_3O_4. The particle size distribution was measured by capillary hydrodynamic fractionation (CHDF). A CHDF-3000 (Matec Applied Science) was used with an operating flow of 1.4 ml/min at 35.0 °C and detector wavelength at 220 nm. The carrier fluid was 1X-GR500 (Matec). The samples were diluted to 0.5% S.C. using the carrier fluid and the samples were analyzed using the Matec software v.2.3. The small population observed around 40 nm which is marked with a star, is an artifact coming from the signal of the emulsifier, which is not separated from the particles due to its small size. Furthermore, the particles containing 5.0 wt% of iron oxide (blue line) show a small peak around 150 nm which probably comes from an artefact as the measurement was performed three times and the peak was only observed once.

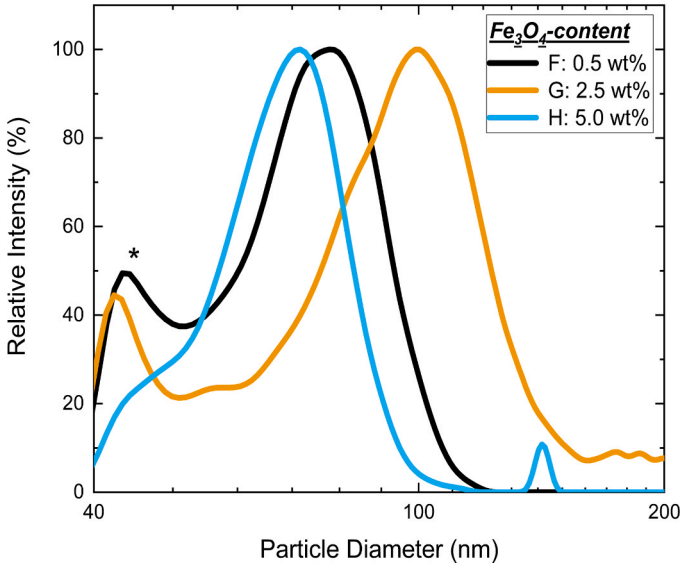

Fig. 4. Particle size distribution of Fe_3O_4–polystyrene latex particles containing 0.5 wt% (black), 2.5 wt% (orange) and 5 wt% (blue) of Fe_3O_4 respectively. The small population observed around 40 nm which is marked with a star, is an artifact due to the signal of the emulsifier, which is not separated from the particles due to its small size.

Scanning transmission electron microscopy (STEM) images of the latex particles containing 7.5 wt% of iron oxide (E in Table 1) are shown in Fig. 5a. In this image, latex particles appear as light gray while iron oxide appears white. The figure shows individual iron oxide latex particles embedded within the latex particles. Using these images, a particles size distribution was obtained for the iron oxide particles which are shown in Fig. 5b.

3.2. Characterization of the membrane samples

To characterize the membrane samples, the pore size distributions were measured, as depicted in Fig. 6a. The data was obtained using mercury intrusion porosometry (MIP). The pore radius deduced from these measurements were 0.42 µm for nylon-membrane I and 0.53 µm for nylon-membrane II, which showed a slight deviation from the specified values of the supplier. Furthermore, Fig. 6b presents a scanning electron microscopy (SEM) image of the top surface of the nylon membrane II.

3.3. Characterization of the liquid solutions

The liquids used in the penetration experiments of Section 3.2 are given in Table 2, together with their physical parameters. For the complete set of liquids used in signal calibration in Section 3.1, we refer to Appendix C. The viscosities of the solutions were measured using an

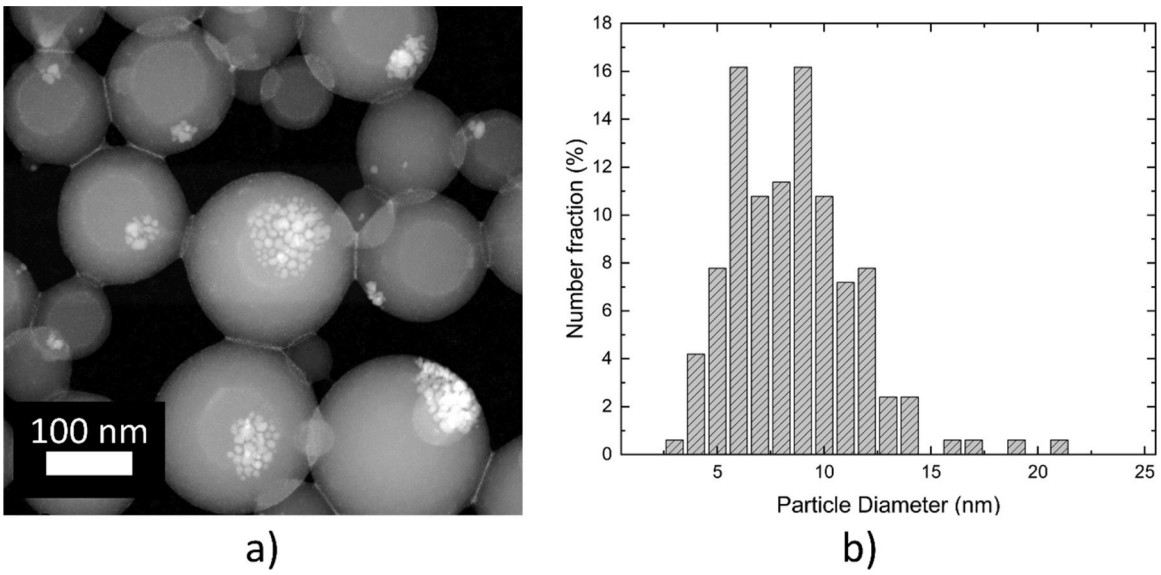

Fig. 5. a) STEM image of the Fe_3O_4 latex particles containing 7.5 wt% iron oxide (E) latex appears as light gray while Fe_3O_4 appears white. B) Particle size distributions of the Fe_3O_4 particles, determined from STEM images.

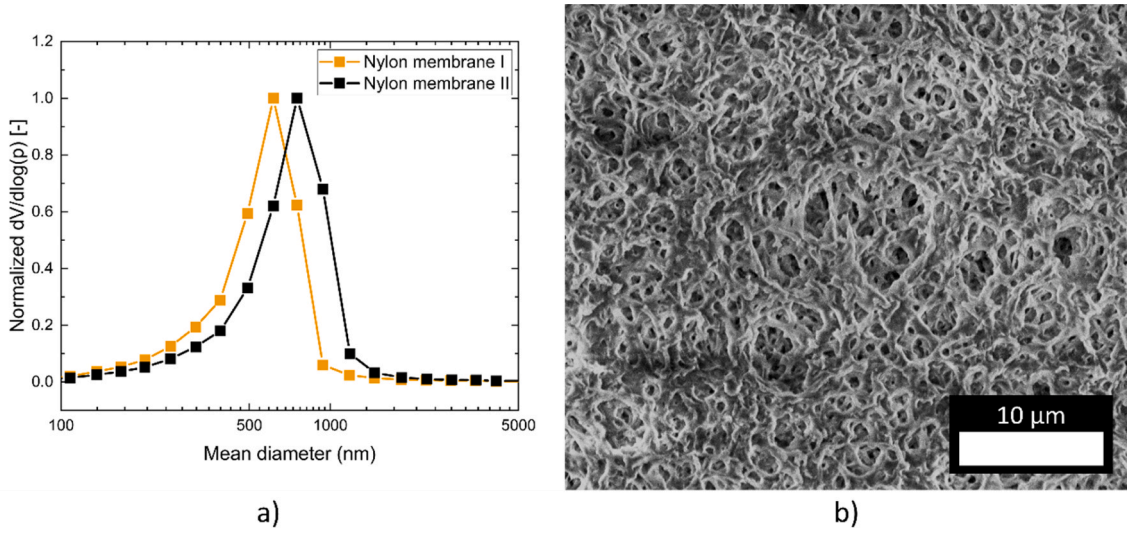

Fig. 6. a) Pore size distribution measured by mercury intrusion porosometry for nylon membrane I and nylon membrane II. b) SEM image of the top surface of nylon membrane II.

Table 2
The liquids used in the imbibition experiments and their physical properties.

Name	Particles (wt%)	Viscosity (mPa.s)	Surface tension (mN/m)	T_1 (ms)	T_2 (ms)
G70P0	0.00	23.48	67.60	6.06	4.95
G70P1F0.5	0.99	25.66	63.48	5.37	3.27
G70P2F0.5	2.10	39.09	59.07	5.46	2.51
G70P3F0.5	3.01	32.79	58.80	5.20	2.11
G70P5F0.5	5.03	39.89	57.74	4.52	1.48
G70P8F0.5	7.94	60.27	55.91	3.40	1.10

Anton Paar MCR302 rheometer (20 °C), while the surface tension was determined using the Wilhelmy plate method.

The measured data reveals that an increase in particle concentration leads to an increased viscosity and decreased surface tension, see Table 2. The T_1 and T_2 times of the liquid solutions are measured using a saturation recovery and OW sequence respectively.

3.4. NMR-characteristics of latex particles

Before particles can be followed during imbibition experiments, their NMR characteristics were studied by determining their relaxation characteristics and effect on the signal intensities within the setup. The goal of this section is to select the proper Fe_3O_4 latex particle and make particle calibration curves. The section starts by determining the relaxation behavior of latex particles containing varying Fe_3O_4-content. Thereafter, the effect of the latex particle concentration on the T_2-relaxation time is studied in order to get values for R_2 and a (Eq. 4). The relaxation measurements will be used to determine the calibration curves and select the Fe_3O_4-latex particles for the imbibition experiments.

3.4.1. Effect of Fe_3O_4-content on the relaxation behavior

To characterize the effect of the iron-oxide within the latex particles, the relaxation characteristics of particles containing different amounts of iron-oxide were measured. All solutions contained 70 wt% water and

30 wt% solid content, from which 0.1 wt% to 7.5 wt% was iron oxide. T_2- and T_1- decay curves were measured using an OW-sequence and saturation recovery sequence. Figures of the decay curves can be found in Appendix A, Fig. 14. The curves show that increasing the iron-oxide content decreases both the T_1- and T_2- relaxation times. In Fig. 7, the inverse relaxation times are plotted as a function of the Fe3O4 content, which shows a linear relationship between both. From this linear relationship, the relaxation rates R_2 and R_1 were determined to be 1.5 $ms^{-1}wt\%^{-1}$ and 0.034 $ms^{-1}wt\%^{-1}$. Based on this finding, the particles containing 0.5, 2.5 and 5 wt% of Fe3O4 were selected for further observation. The particles containing 0.1 wt% showed a T_2- relaxation time with too low effect to make them clearly visible, whereas the one containing 7.5 wt% decreased the T_2-relaxation time too much in order to have sufficient signal for UFI measurements.

3.4.2. *Effect of particle concentration on the relaxation behavior*

To determine the relaxation characteristics as function of the particle concentration, relaxation times were determined for liquid mixtures containing varying particle concentrations. Because the addition of Clariscan will ensure that the T_1-relaxation time will not influence the signal intensity (Eq. 1), only the T_2 decay will be discussed in this section. Information about the effect on the T_1-relaxation time can be found in Appendix B. This study was performed on solutions containing a varying glycerol content (0 wt%, 25 wt%, 50 wt% and 70 wt%) with the particles containing 0.5 wt%, 2.5 wt% and 5 wt% of iron oxide. A list of all solutions can be found in Appendix C. T_2-relaxation times of the solutions were determined by an Ostroff-Waugh pulse sequence with an echo time of 50 μs. The measured decay curves for the solution containing 70 wt% glycerol, 0.005 M Clariscan and 0 - 8 wt% of particles are given in Appendix B, Fig. 15. Fig. 8 shows the inverse T_2 relaxation time and maximum signal intensity as a function of particle concentration (particles with 0.5 wt% of iron oxide) for a mixture containing 70 wt% of glycerol. These dispersions will be used for penetration experiments in Section 3.2. It is obviously, increasing the particle concentration increases the inverse T_2-relaxation time, as expected from Eq. 2. The expected linear relationship between $1/T_2$ and the particle concentration is observed. Furthermore, the maximum signal intensity depends linearly on the particle concentration. Using these data, a value for the density change factor a (0.016 $wt\%^{-1}$) and relaxivity R_2 (0.042 $ms.wt\%^{-1}$) can be found. Values for a and R_2 corresponding to all possible combinations of glycerol content and iron oxide content can be found in Appendix D.

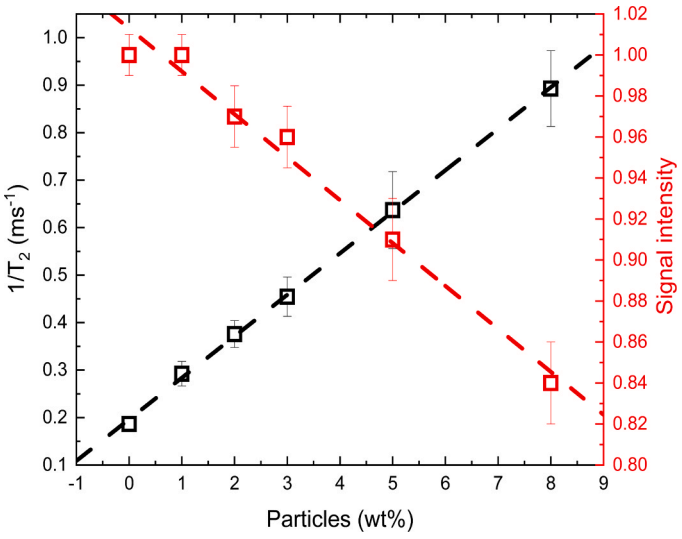

Fig. 8. Inverse -relaxation time (black) and maximum signal intensity (red) in function of particle concentration for a dispersion containing 70 wt% of glycerol and particles with 0.5 wt% of Fe_3O_4.

3.4.3. *Calibration curves*

In this section, the previous measured relaxation characteristics will be used to construct calibration curves that couple the signal intensity with the particle concentration in UFI-NMR experiments. These calibration curves allow to determine particle density profiles during capillary uptake.

In this section, calibration curves are determined for solutions containing 70 wt% glycerol and iron oxide contents of 0.5, 2.5 and 5 wt%. Calibration curves for other combinations of glycerol and iron oxides contents can be found in Appendix D. To test the theoretical model, signal intensities of all liquid mixtures were measured by UFI-NMR. Fig. 9 shows a comparison between the measured signal intensities (dots) and the predictions (lines) using the theoretical model.

The graph shows the calibration curve for different Fe_3O_4 latex particles, containing 0.5 wt%, 2.5 wt% and 5 wt% of Fe_3O_4. As expected, with increasing the Fe_3O_4 content, the signal drop is steeper with increasing the particle concentration. It is seen that the measured signal intensities (points) coincide very well with the theoretical signal intensities (lines) found by Eq. 1. The type of Fe_3O_4-content that should be used will depend on the type of experiment. The advantage of using a lower iron oxide content, such as 0.5 wt%, is the large range of particle

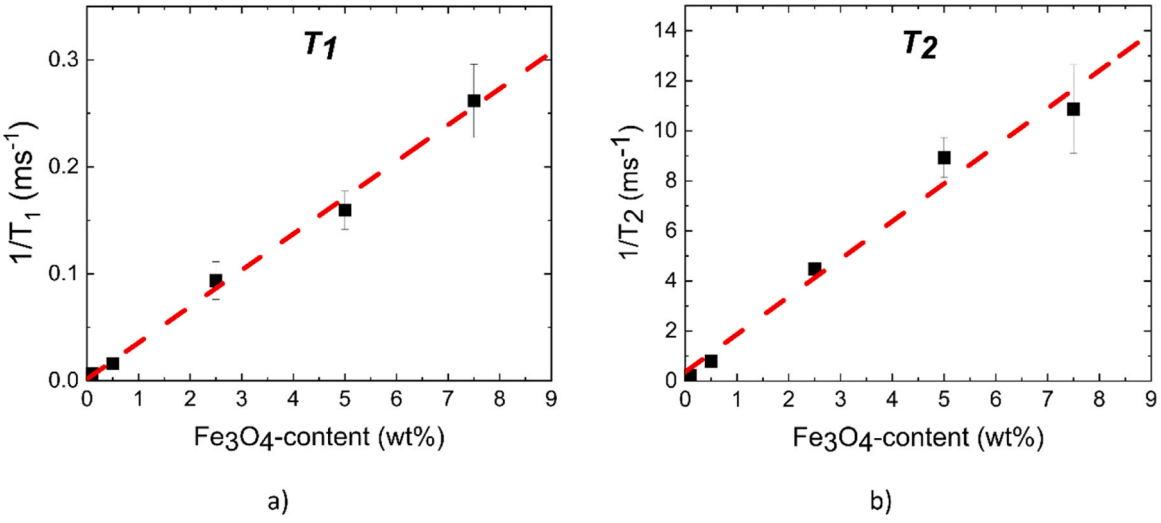

Fig. 7. Inverse relaxation times as a function of the Fe_3O_4-content in the latex particles cores. a) T_1 and b) T_2.

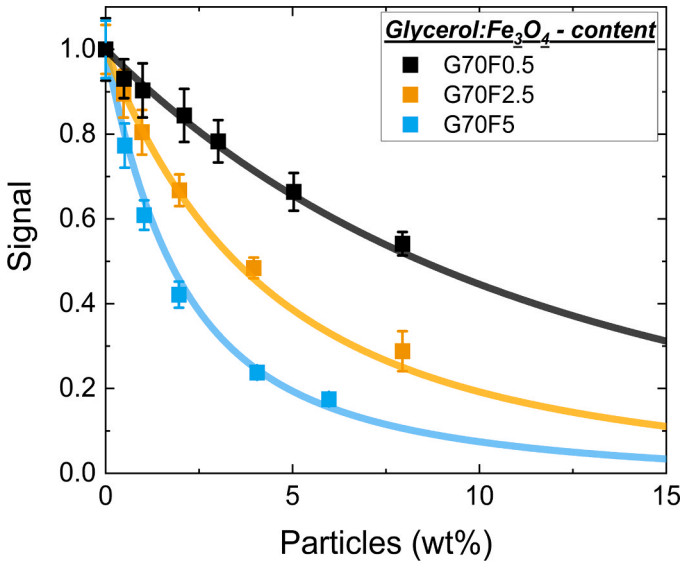

Fig. 9. Calibration curves for the signal intensity in function of the particle concentration for varying Fe_3O_4 contents but with the same glycerol content of 70 wt%. Calibration curves, predicted from the previously obtained values of R_2 and a, are shown as lines. The data points mark measured UFI-NMR signals from the particle dispersions.

concentrations that can be probed. However, the signal differences are smaller and therefore harder to discriminate. Therefore, when small particle concentrations should be discriminated, particles with a higher Fe_3O_4 content are recommended. The downside of the larger signal differences is the smaller range of particle concentrations that can be probed. While with a 0.5 wt% Fe_3O_4 content, solution with a particle concentration of 15 wt% still provide enough signal (black line), the particles with 2.5 wt% (orange line) and 5 wt% (blue line) can only be used to probe particle concentrations up until 7.5 wt%, where the signal enters the noise level. In the subsequent study, we performed all measurements on dispersion with particles containing 0.5 wt% Fe_3O_4.

3.5. Measuring particle concentration profiles during imbibition

In this section, it will be shown that the UFI-NMR method can be used to study particle transport during imbibition. This is done by comparing two imbibition experiments on a nylon 0.45 membrane. One experiment is performed with a solution containing no particles (G70P0) while the other one contains 5 wt% of particles (G70P5F0.5). Both solutions contain 70 wt% of glycerol to slow down the penetration and increase the signal-to-noise ratio. The section starts by comparing the measured UFI-NMR signal intensity profiles for both experiments. Thereafter, the calibration curves in Fig. 9 will be used to determine particle concentration profiles, which in the final part will be compared to SEM-images.

Fig. 10a, shows the liquid profiles for the G70P0 liquid. Similar profiles were also measured in a previous study, with the penetration of a glycerol mixture inside PVDF and nylon membranes [28,29]. The liquid profiles can be divided in three main regions which by moving from left to right are: the droplet ($S = 1$), membrane ($S \approx 0.65$) and tape ($S = 0$). In the case of no particles, Fig. 10a, the droplet ($x < 0$) has signal intensity 1, referring to a fully saturated region. Inside the membrane ($0 < x < 170$), the volume percentage of liquid drops, because of the membrane porosity. This results in a decrease in signal intensity equal to the porosity of the membrane, which in this membrane is around 65%. The tape ($170 < x$) has signal intensity of 0 because of the absence of liquid.

Fig. 10b, shows the liquid profiles for the penetration of the G70P5F0.5 liquid. The liquid profiles are shown in a wide range of timesteps, indicated with a green color map. Here, profiles are measured for longer times than in Fig. 10a, because particles keep penetrating after the liquid had reached the bottom of the membrane. The addition of particles will affect the measured liquid profiles (blue arrows). For comparison a liquid profile of a fully saturated membrane containing the G70P0 is added (orange). As expected, the signal inside the droplet decreases from 1 to 0.65, in correspondence with the black calibration curve in Fig. 9. Inside the membrane, the signal intensity drop appears in the upper part of the membrane ($0 < x < 100$) while, in the bottom part of the membrane ($x > 100$) the signal intensity increases again. These profiles correspond to case C from Fig. 2, the situation that the particle front lags behind the liquid front. A clear signal increase is only observed behind 100 μm, which indicates that the splitting before this distance is not large enough to be picked up by our setup. The particle's final penetration depth can be determined to be 100 μm, the position where the signal intensity starts to increase again. After the liquid has reached the bottom of the membrane, the droplet keeps spreading, allowing more particles to enter inside the membrane. The increase in particle concentration within the membrane can be observed by the decrease in signal intensity (black arrows). Besides the signal increase within the membrane, also a slight signal decrease on top of the membrane is observed, which is probably due to a buildup of particles that are unable to penetrate inside the medium.

Using the black calibration curve in Fig. 9, particle density profiles can be calculated for every signal profile shown in Fig. 10b. However, before this can be done, the effect of porosity on the signal intensity

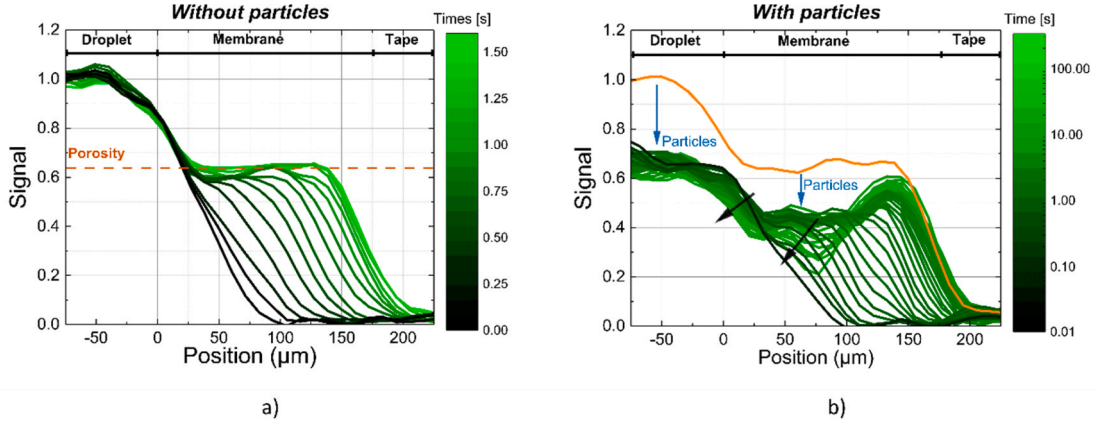

Fig. 10. UFI-NMR signal profiles measured for different times during the penetration of a 70 wt% glycerol mixtures with no particles (a) and with 5 wt% of Fe_3O_4-latex particles that contain 0.5 wt% of Fe_3O_4 (b) inside nylon membrane II. A green color map is used to mark the specific time of each profile. Note the huge time difference in timescales of both figures.

should be taken into account. This is done by dividing the signal profiles of Fig. 10b (green) by a profile of a fully saturated membrane (orange) containing only liquid. This will result in signal intensity profiles that are completely determined by the particle concentration, for which the calibration curve can be used to determine the particle concentration profiles. Fig. 11, shows the particle concentration profiles that correspond to the signal profiles shown in Fig. 10b. However, there are still some limitations when determining the particle concentration profiles. First, the particle concentration can only be determined behind the liquid front, where the signal intensity has reached its maximum and is not affected by the limits in resolution. If concentrations are determined too close to the liquid front, the incline due to the resolution limit will result in an overestimation of the particle concentration. Therefore, particle concentrations are determined until 20 μm behind the liquid front. For the same reason, particle concentration profiles are only shown until 175 μm. However, some profiles still have the problem of an overestimation near the end of the particle concentration profiles. The resolution problems will also lead to difficulties in determining particle concentrations near the droplet-membrane interface.

The particle concentration profiles in Fig. 11 show that the particle concentration inside the droplet and top part of the membrane varies around 5 wt%, in line with the initial concentration of the droplet. This shows that the particles are not hindered by the interface and move together inside the porous medium. This small decline observed at the droplet-membrane interface is probably due to difficulties in determining the particle concentration around interfaces, as it will become more homogeneous through time. During penetration, it is observed that the particle concentration will start to decrease around 100 μm. However, the particle concentration does not decrease towards 0, which suggest that some particles penetrate deeper than 100 μm. Another explanation may originate from the NMR-resolution. If the experimental resolution is 18 μm, a complete signal recovery would require that the particles are at least 36 μm separated from the end of the membrane. In practice, this distance to require complete signal recovery can be somewhat higher. However, our measurement, shows that particles are able to penetrate up to 100 μm and the sample is around 170 μm in thickness. Therefore, there are probably particles that do penetrate a little further than 100 μm.

After the liquid has reach the end of the membrane, the continuous spreading of the droplet in lateral direction will keep bringing particles into the membrane. Because the lateral penetration of liquid takes place beyond the measurements area, this movement cannot be observed within the UFI measurement, see Fig. 3. However, the additional particles that are brought in are observed by an increase in the particle concentration, which is marked by black arrows in Fig. 11. It is seen that the particle concentration does not increase homogeneously throughout the medium. The concentration increases first inside the membrane, at 100 μm, which is the depth the particles could penetrate during the process of vertical liquid penetration. Followed by a particle concentration increase that will travel towards the droplet-membrane interface. The final profiles show that the particle concentration has increased to 12 wt% within 330 s

To verify these findings, SEM-images of the samples cross-section were taken after penetration. Fig. 12 a and b show the SEM-images, corresponding to the samples used for the experiments shown in Fig. 10a (no particles) and Fig. 10b (5 wt% of particles). In samples without particles (reference), the membranes texture is homogeneous throughout the whole cross-section. No particles are visible and only nylon fibers can be seen. The situation is completely different after the penetration of a dispersion containing 5 wt% of particles (Fig. 12b). Based on the texture, three different regions can be distinguished. The top, which looks denser and completely different than the reference sample, the middle, appearing even denser (between white dashed lines) and the bottom with a similar texture as the reference sample. Fig. 13 shows close-up pictures of the top (a), middle (b) and bottom (c) part of the picture in Fig. 12b. In the top of the membrane, particles are clearly visible. The particles cover the entire surface of the nylon membrane and almost no fibers are visible. Particles are also visible in the middle part of the membrane, but here the density of particles is higher compared to the top part. Whereas open pores are still visible at the top of the membrane, almost no open pores are visible in the middle part of the membrane. From the SEM pictures, the dense particle layer is determined to have a thickness around 30 μm, white dashed lines in Fig. 12b. The gradient in particle concentration, as well as the dense particle layer, are in line with the observation made by the UFI-NMR experiment in Fig. 11. Where particles are present at the top and middle part of the membrane, they are not visible in the bottom part, Fig. 13c. This underlines the existence of a final particle penetration depth, in line with the UFI-NMR observation. The final penetration depth extracted from the SEM images is 95 μm (indicated with a white arrow). A closer look to

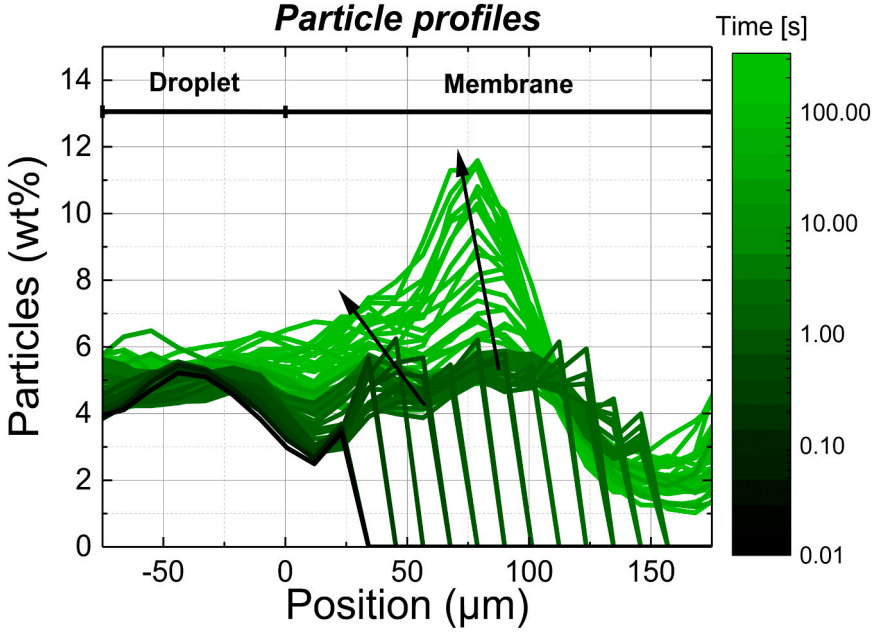

Fig. 11. Particle concentration profiles that correspond the signal profiles of Fig. 10b.

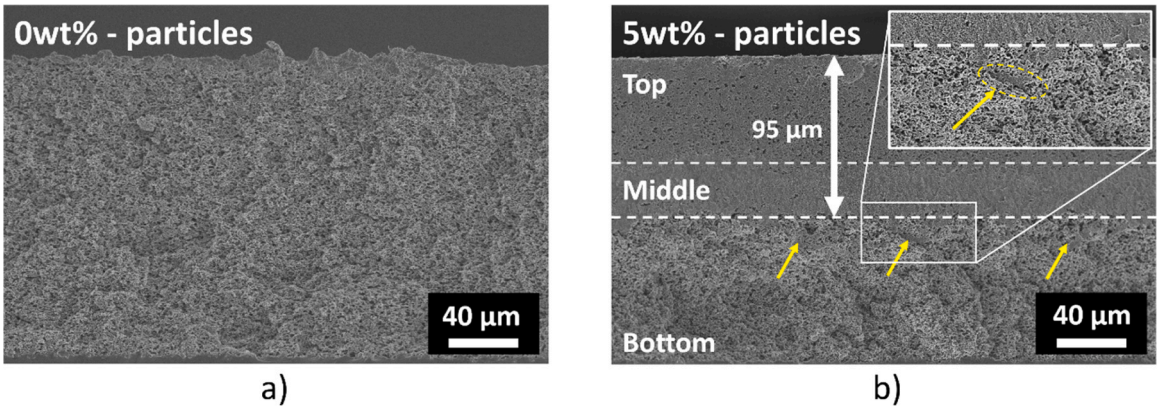

Fig. 12. SEM-images of the cross section of a nylon membrane after the penetration of a droplet containing no particles (a) and containing 5 wt% of particles (b). Both droplets also contained 70 wt% of glycerol. The white line marks the particle penetration depth and the red lines refer to particles that were able to penetrate behind the final particle penetration depth.

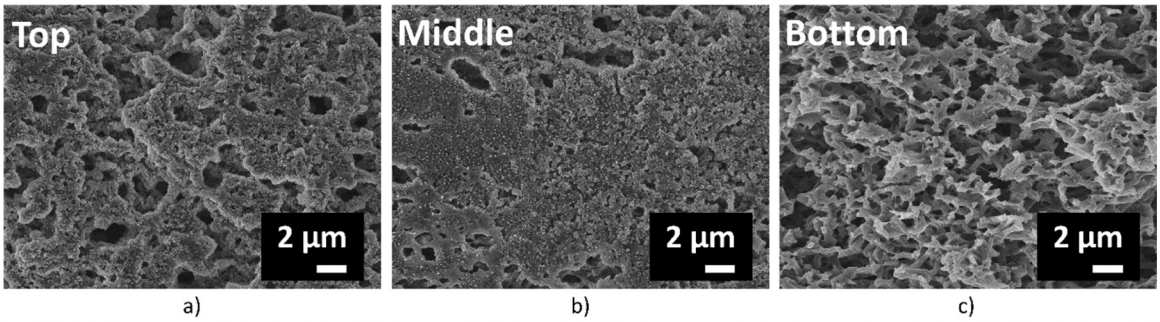

Fig. 13. SEM images of the top (a), middle (b) and bottom (c) part of the cross-section shown in Fig. 12b.

Fig. 12b, reveals that there are some particles beyond the dense particle layer (red arrows). This is probably the reason for the non-zero particle concentration found beyond 100 µm in Fig. 11.

4. Conclusions

In this paper, it is demonstrated how a previously introduced Ultra-Fast Imaging NMR method (UFI) allows to study particle transport in thin, porous membranes. The study started with an extensive explanation about the effect of Fe_3O_4-latex particles on the UFI-NMR signal. In this part, a calibration curve was found that linked the UFI-NMR signal to the particles concentration. The curves showed that Fe_3O_4-latex particles will decrease the UFI-NMR signal due to T_2-relaxation and lowering the water molecule fraction.

The second part, demonstrates how UFI-NMR can be used to study the particle penetration during imbibition into thin, porous media. UFI-NMR measurements of the penetration of a 70 wt% glycerol mixture containing 5 wt% of Fe_3O_4-latex particles revealed that the particles were able to penetrate inside a 170 µm thick nylon membrane. The measurements also showed a splitting between the liquid and particle front, which resulted in a final particle penetration depth of 100 µm. The UFI-NMR profiles could be used to determine particle concentration profiles during penetration, revealing an inhomogeneous buildup of particles within the membrane. The concentration increases first within the membrane, at the final particle penetration depth of 100 µm, after which the concentration also increases more at the top of the membrane. The measurements showed that the particle concentration has increased from 5 to 12 wt% within 330 s within the membrane.

Both the final particle penetration depth and gradient in particle concentration were verified with Scanning Electron Microscopy images of the samples.

CRediT authorship contribution statement

R.J.K. Nicasy: Conceptualization, Data curation, Formal Analysis, Investigation, Methodology, Visualization, Writing – original draft. **A. Barquero**: Writing – review & editing, Resources, Investigation. **S.J.F. Erich**: Conceptualization, Supervision, Writing – review & editing. **O.C. G. Adan**: Funding acquisition, Project administration, Supervision, Writing – review & editing. **H. Mansouri**: Investigation, resources. **N. Tomozeiu**: Resources, supervision, writing – review & editing. **J. Scheerder**: Resources, supervision, writing – review & editing. **H.P. Huinink**: Conceptualization, Funding acquisition, Project administration, Supervision Writing – review & editing.

Declaration of Competing Interest

The authors declare that they have no known competing financial interests or personal relationships that could have appeared to influence the work reported in this paper.

Data availability

Data will be made available on request.

Acknowledgements

This publication is part of the project PQP (Print Quality and Particles) (Project No. 17099) of the research collaboration program High Tech Systemen en Materialen (HTSM) 2018 TTW, which was (partly) financed by the Dutch Research Council (NWO). The researchers would also like to thank H. Dalderop (TU/e) and M. Kurvers (TU/e) for helping to build the experimental setup. We acknowledge P. Lipman (TU/e) for

doing the MIP measurements, H. Koier (CPP) for the viscosity and R. Vanos (CPP) for the surface tension measurements. Last, we would like to thank Covestro and Canon Production Printing for their support.

Appendix A. NMR decay curves in function of Fe_3O_4 content within the latex particles

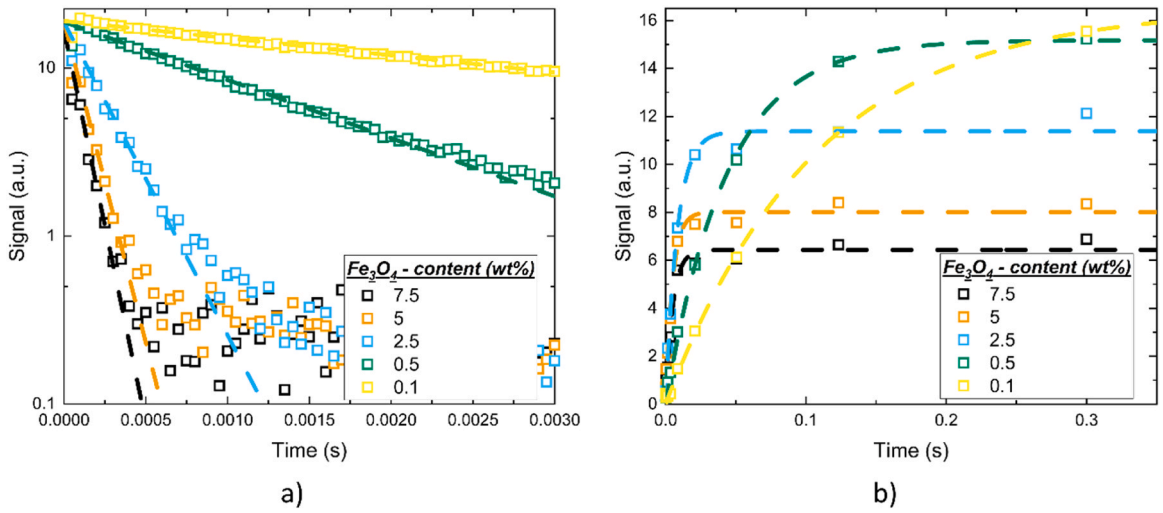

Fig. 14. a) T_2 relaxation measurement performed by an OW-sequence for solutions containing 30 wt% of latex particles with varying Fe_3O_4 content ranging between 0.1 and 7.5 wt%. Dots are used for measured data while lines are the corresponding fits. b) T_1 relaxation measurements performed by a saturation recovery sequence on the same solutions found in figure a.

.

To study the effect of Fe_3O_4 within the latex particles on the NMR relaxation times of the liquid dispersion, signal decays were measured by an OW-sequence($t_e = 50\mu s$) for the T_2-time and by a saturation recovery sequence for the T_1-time. Fig. 14 shows measured signal decays for the T_2 measurement (a) and the T_1 measurement (b) for solution containing 30 wt% of Fe_3O_4-latex particles with varying iron oxide contents between 0.1 and 7.5 wt%. In both cases, increasing the Fe_3O_4 content increases the signal decay rates. Decay curves of the data are fitted with dotted lines and can be used to extract the T_2- (Figure 7b) and T_1-time (Fig. 7a) Besides the changes in relaxation time, it is observed that by increasing the Fe_3O_4 content, the maximum NMR-signal decreases. The decreasing NMR signal can partly be understood by the replacement of polystyrene with iron oxide which lowers the hydrogen atom density. However, the signal change is larger than would be expected based on only the replacement of polystyrene with iron oxide. A possible reason for this behavior would be that the iron oxide bleaches part of the signal around it. Further research is required to quantify this effect, but this lies beyond the scope of this research and is therefore not given.

Appendix B. Decay curves in function of particle concentration

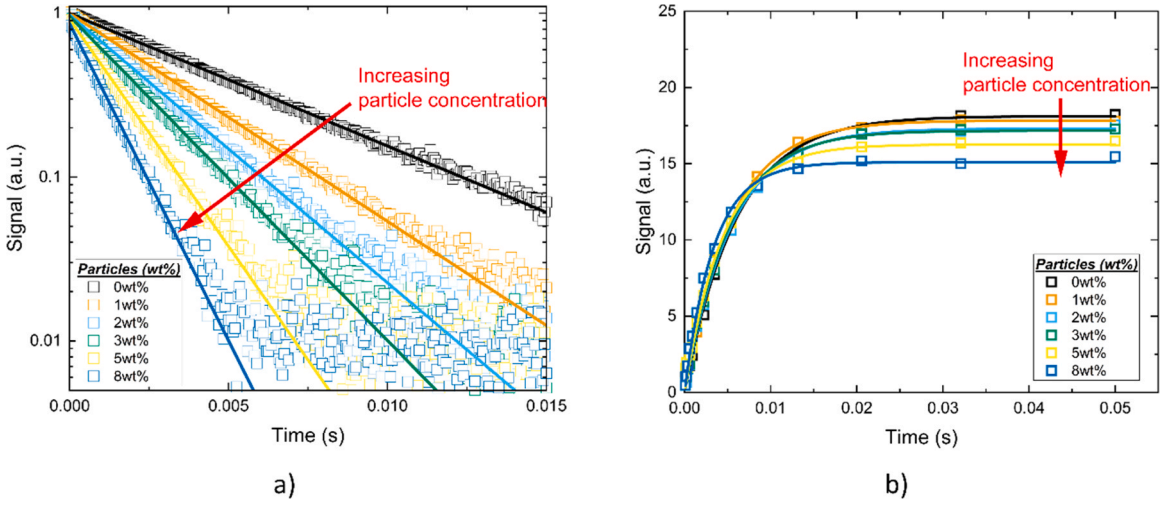

Fig. 15. a) Signal decays measured by an OW-sequence for liquid solutions containing varying amounts of latex particles, 70 wt% of glycerol and 0.5 wt% Fe_3O_4. B) Signal decays measured by a saturation recovery sequence for liquid solutions containing varying amounts of latex particles, 70 wt% of glycerol and 0.5 wt% Fe_3O_4.

.

In this section, the NMR T_2 and T_1 decay curves are shown for solutions containing 70 wt% glycerol, 0.005 M Clariscan and varying particle concentrations. The particles in the measurements that are shown contain 0.5 wt% of iron oxide. The data is measured with an OW-sequence ($t_e = 50\mu s$) and saturation recovery sequence for the T_2 and T_1 respectively. Fig. 15 shows the signal decay curves for T_2 (a) and T_1 (b). By fitting the

relaxation data with $S = S_{max}\exp(-t/T_2)$ and $S = S_{max}(1 - \exp(-t/T_1))$, the relaxation data and maximum signal intensities can be extracted. For the T_2-decays, fits were made on the first 32 echoes. The reason for choosing only the first 32 echoes is because UFI uses the first 32 echoes to build up a liquid profile [29]. Therefore, the relaxation characteristics of these first 32 points are most relevant and are used for fitting. In both measurements, the relaxation time and maximum signal intensity decreases when increasing the particle concentration, marked by a red arrow.

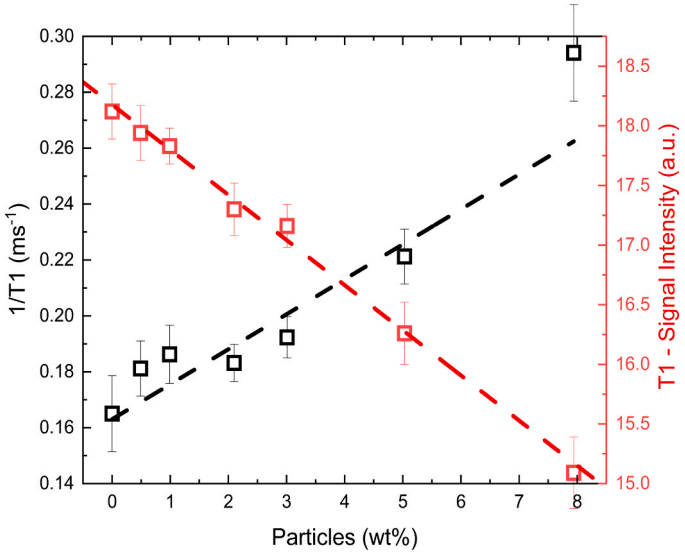

Fig. 16. Inverse T1-relaxation time and maximum signal intensity in function of particle concentration for a solution containing 70 wt% of glycerol and Fe3O4-latex particles with 0.5 wt% of iron oxide.

.

The determined relaxation times and maximum signal intensities can be used to determine the relaxation rates (R_1, R_2) and required for Eq. 4. The value for R_2 is determined in section 3.1.2 Fig. 8 while the value for R_1 is determined within this section Fig. 16.

In this section, relaxation parameters are determined for Fe_3O_4-latex particles with an iron oxide content of 0.5 wt% in a solution containing 70 wt % glycerol and 0.005 M Clariscan. However, this procedure was repeated to determine the relaxation characteristics of the Fe_3O_4-latex particles in varying glycerol contents (0, 25, 50 and 70 wt%) and with varying iron oxide contents (0.5, 2.5 and 5 wt%).

Table 3
Relaxivities (R_1 and R_2) and density change factor () for three different Fe_3O_4-latex particles with varying iron oxide contents (0.5, 2.5 and 5 w%) in varying glycerol content environments (0, 25, 50 and 70 wt%).

Glycerol content (wt%)	Fe_3O_4 content (wt%)	a ($wt\%^{-1}$)	R_2 ($ms.wt\%^{-1}$)	R_1 ($ms.wt\%^{-1}$)
0	0.5	0.011	0.042	0.003
	2.5	0.017	0.24	0.005
	5	0.026	0.40	0.007
25	0.5	0.012	0.06	0.005
	2.5	0.017	0.28	0.005
	5	0.025	0.50	0.008
50	0.5	0.013	0.088	0.005
	2.5	0.020	0.32	0.006
	5	0.028	0.58	0.006
70	0.5	0.016	0.095	0.013
	2.5	0.026	0.26	0.009
	5	0.035	0.54	0.014

Appendix C. NMR characteristics of liquid solutions

In this appendix, all liquid mixtures used within this study are listed. The mixtures vary in glycerol content (0 wt%, 25 wt%, 50 wt% and 70 wt%), Fe_3O_4 latex particles (containing 0.5 wt%, 2.5 wt% or 5 wt% of iron oxide) and Clariscan concentration. Solutions were coded by GxPyFz, where x gives the wt% of glycerol, y the wt% of particles and z the wt% of iron oxide. For every liquid, the particle concentration is given together with the T_1- and T_2 relaxation time in ms. Besides the relaxation times, also the maximum signal intensities (T_{2max} and T_{1max}) for both the T_1-and T_2-measurement are given. All data shows that increasing the particle concentration will lower the relaxation time and maximum signal intensities as explained in section 3.1.2.

Table 4
Dispersions contain the Fe_3O_4-latex particles with 0.5 wt% of iron oxide content and 0 (a), 25 (b), 50 (c) and 70 wt% (d) of glycerol. The corresponding Clariscan concentrations are 0.04 M (a), 0.02 M (b), 0.01 M (c) and 0.008 M (d).

Name	Particles (wt%)	T_1 (ms)	T_2 (ms)	T_{1max} (a.u.)	T_{2max} (a.u.)	Name	Particles (wt%)	T_1 (ms)	T_2 (ms)	T_{1max} (a.u.)	T_{2max} (a.u.)
G0P0	0	5.89	3.05	18.01	23.47	G25P0	0	6.67	3.79	17.95	23.63
G0P1F0.5	1.02	5.71	2.71	17.68	23.27	G25P1F0.5	1.03	6.37	3.16	17.83	23.55
G0P3F0.5	2.99	5.46	2.21	17.20	22.89	G25P2F0.5	2.03	6.3	2.7	17.61	23.24
G0P5F0.5	4.98	5.63	1.89	16.75	22.21	G25P4F0.5	3.01	6.08	2.04	16.98	22.72
G0P7F0.5	7.01	5.30	1.6	16.27	21.89	G25P8F0.5	5.03	5.69	1.38	15.97	21.49
G0P10F0.5	10.03	5.08	1.33	15.69	21.04	G25P15F0.5	7.94	4.21	0.81	14.07	19.48
G0P15F0.5	14.95	4.60	1.03	14.47	19.07						
		a)							b)		
Name	**Particles (wt%)**	**T_1 (ms)**	**T_2 (ms)**	**T_{1max} (a.u.)**	**T_{2max} (a.u.)**	**Name**	**Particles (wt%)**	**T_1 (ms)**	**T_2 (ms)**	**T_{1max} (a.u.)**	**T_{2max} (a.u.)**
G50P0	0	8.53	6.00	24.77	25.43	G70P0	0	6.06	5.36	18.12	23.34
G50P1F0.5	1.02	7.21	3.77	24.03	25.02	G70P0.5F0.5	0.49	5.52	4.00	17.94	23.36
G50P3F0.5	2.95	5.65	2.22	23.02	24.24	G70P1F0.5	0.99	5.37	3.42	17.83	23.23
G50P5F0.5	5.01	6.67	1.72	22.34	23.60	G70P2F0.5	2.10	5.46	2.66	17.3	22.75
G50P8F0.5	8.00	6.55	1.22	21.15	22.62	G70P3F0.5	3.01	5.2	2.22	17.16	22.24
G50P10F0.5	9.95	5.36	1.00	20.38	21.82	G70P5F0.5	5.03	4.52	1.57	16.26	21.52
G50P14F0.5	14.11	5.4	0.74	19.15	20.93	G70P8F0.5	7.94	3.4	1.22	15.09	20.19
		c)							d)		

Table 5
Dispersions contain the Fe_3O_4-latex particles with 2.5 wt% of iron oxide content and 0 (a), 25 (b), 50 (c) and 70 wt% (d) of glycerol. The corresponding Clariscan concentrations are 0.04 M (a), 0.01 M (b), 0.008 M (c) and 0.005 M (d).

Name	Particles (wt%)	T_1 (ms)	T_2 (ms)	T_{1max} (a.u.)	T_{2max} (a.u.)	Name	Particles (wt%)	T_1 (ms)	T_2 (ms)	T_{1max} (a.u.)	T_{2max} (a.u.)
G0P0	0	5.89	3.05	18.01	23.47	G25P0	0	14.54	5.75	18.50	23.57
G0P1F2.5	1.00	5.87	1.80	17.34	22.69	G25P1F2.5	1.00	12.58	2.14	17.60	23.19
G0P2F2.5	2.03	5.74	1.22	16.85	22.65	G25P2F2.5	2.00	12.53	1.34	16.96	22.74
G0P3F2.5	3.03	5.75	0.95	16.38	22.36	G25P4F2.5	4.02	11.07	0.78	15.80	21.75
G0P4F2.5	4.05	5.47	0.76	15.74	21.86	G25P8F2.5	7.97	9.53	0.43	13.97	20.28
G0P5F2.5	5.05	5.28	0.64	15.32	21.34	G25P16F2.5	16.07	6.67	0.22	10.48	17.90
G0P7F2.5	7.05	4.94	0.49	14.24	20.45						
		a)							b)		
Name	**Particles (wt%)**	**T_1 (ms)**	**T_2 (ms)**	**T_{1max} (a.u.)**	**T_{2max} (a.u.)**	**Name**	**Particles (wt%)**	**T_1 (ms)**	**T_2 (ms)**	**T_{1max} (a.u.)**	**T_{2max} (a.u.)**
G50P0	0	7.78	5.49	17.97	23.39	G70P0	0	5.51	4.41	17.53	22.98
G50P1F2.5	0.99	7.32	1.94	17.30	22.93	G70P1F2.5	0.48	5.62	2.65	17.29	22.64
G50P2F2.5	1.94	6.89	1.22	16.78	22.58	G70P2F2.5	0.97	5.21	1.99	16.95	22.21
G50P4F2.5	4.02	6.6	0.70	15.39	21.27	G70P4F2.5	1.97	5.20	1.30	16.33	21.58
G50P8F2.5	7.99	5.2	0.39	13.37	19.43	G70P8F2.5	3.96	4.41	0.81	15.12	20.19
G50P12F2.5	11.91	4.81	0.27	11.65	18.03	G70P12F2.5	7.94	4.13	0.47	13.51	18.02
		c)							d)		

Table 6
Dispersions contain the Fe_3O_4-latex particles with 5 wt% of iron oxide content and 0 (a), 25 (b), 50 (c) and 70 wt% (d) of glycerol. The corresponding Clariscan concentrations are 0.04 M (a), 0.02 M (b), 0.008 M (c) and 0.006 M (d).

Name	Particles (wt%)	T_1 (ms)	T_2 (ms)	T_{1max} (a.u.)	T_{2max} (a.u.)	Name	Particles (wt%)	T_1 (ms)	T_2 (ms)	T_{1max} (a.u.)	T_{2max} (a.u.)
G0P0	0	6.17	3.07	17.66	23.15	G25P0	0	6.46	3.82	17.74	23.13
G0P0.5F5	0.47	6.32	1.99	17.33	22.58	G25P0.5F5	0.53	6.59	1.86	17.22	22.83
G0P1F5	1.00	6.37	1.39	16.87	22.22	G25P1F5	0.99	6.73	1.34	16.89	22.53
G0P2F5	2.04	5.94	0.85	16.27	21.68	G25P2F5	2.00	6.26	0.81	16.05	21.92
G0P4F5	4.04	5.48	0.50	14.94	20.46	G25P4F5	4.01	5.48	0.46	14.42	20.61
G0P6F5	6.11	4.94	0.35	13.66	19.31	G25P6F5	5.94	5.01	0.33	13.12	19.64
		a)							b)		
Name	**Particles (wt%)**	**T_1 (ms)**	**T_2 (ms)**	**T_{1max} (a.u.)**	**T_{2max} (a.u.)**	**Name**	**Particles (wt%)**	**T_1 (ms)**	**T_2 (ms)**	**T_{1max} (a.u.)**	**T_{2max} (a.u.)**
G50P0	0	6.60	4.50	17.51	23.25	G70P0	0	5.01	4.22	17.50	22.64
G50P0.5F5	0.51	6.67	1.90	17.06	22.59	G70P0.5F5	0.51	5.32	1.90	17.03	22.05
G50P1F5	1.03	7.37	1.22	16.75	22.21	G70P1F5	1.03	5.57	1.28	16.38	21.56
G50P2F5	2.02	6.52	0.73	15.83	21.45	G70P2F5	1.96	4.99	0.78	15.70	20.72
G50P4F5	4.03	5.75	0.41	13.80	20.26	G70P4F5	4.05	3.91	0.43	13.92	18.99
G50P6F5	6.04	5.73	0.28	12.44	19.05	G70P6F5	5.97	3.70	0.31	12.53	17.58
		c)							d)		

References

[1] W. Hoffmann, et al., Processing of extended shelf life milk using microfiltration, Int. J. Dairy Technol. vol. 59 (4) (2006) 229–235, https://doi.org/10.1111/J.1471-0307.2006.00275.X.

[2] S.Y. Yang, I. Ryu, H.Y. Kim, J.K. Kim, S.K. Jang, T.P. Russell, Nanoporous membranes with ultrahigh selectivity and flux for the filtration of viruses, Adv. Mater. vol. 18 (6) (2006) 709–712, https://doi.org/10.1002/ADMA.200501500.

[3] J. Chatterjee, S. Pratap, S. Abdulkareem, Dual-deposition rates in colloid filtration caused by coupled heterogeneities in a colloidal population, J. Colloid Interface Sci. vol. 356 (1) (2011) 362–368, https://doi.org/10.1016/J.JCIS.2010.12.029.

[4] B. Jalvo, A. Aguilar-Sanchez, M.X. Ruiz-Caldas, A.P. Mathew, Water filtration membranes based on non-woven cellulose fabrics: Effect of nanopolysaccharide coatings on selective particle rejection, antifouling, and antibacterial properties, Nanomaterials vol. 11 (7) (2021) 1752, https://doi.org/10.3390/NANO11071752/S1.

[5] R. Balamurugan, S. Sundarrajan, S. Ramakrishna, Recent trends in nanofibrous membranes and their suitability for air and water filtrations, vol. 1, no. 3, pp. 232–248, Membr Vol. 1 (2011) *232–248*, https://doi.org/10.3390/MEMBRANES1030232.

[6] A. Benamar, N.D. Ahfir, H.Q. Wang, A. Alem, Particle transport in a saturated porous medium: Pore structure effects, Comptes Rendus - Geosci. vol. 339 (10) (2007) 674–681, https://doi.org/10.1016/J.CRTE.2007.07.012.

[7] T. Ikni, A. Benamar, M. Kadri, N.D. Ahfir, H.Q. Wang, Particle transport within water-saturated porous media: Effect of pore size on retention kinetics and size selection, Comptes Rendus Geosci. vol. 345 (9–10) (2013) 392–400, https://doi.org/10.1016/J.CRTE.2013.09.001.

[8] L.M. McDowell-Boyer, J.R. Hunt, N. Sitar, Particle transport through porous media, Water Resour. Res. vol. 22 (13) (1986) 1901–1921, https://doi.org/10.1029/WR022I013P01901.

[9] X. Wang *et al.*, Surface Wettability for Skin-Interfaced Sensors and Devices, 2022, ⟨doi:10.1002/adfm.202200260⟩.

[10] Y. Liu, et al., Skin-interfaced superhydrophobic insensible sweat sensors for evaluating body thermoregulation and skin barrier functions, ACS Nano vol. 17 (6) (2023) 5588–5599, https://doi.org/10.1021/ACSNANO.2C11267/SUPPL_FILE/NN2C11267_SI_002.MP4.

[11] W. Liu, H. Cheng, X. Wang, Skin-interfaced colorimetric microfluidic devices for on-demand sweat analysis, npj Flex. Electron. vol. 7 (1) (2023), 43, https://doi.org/10.1038/s41528-023-00275-y.

[12] P.J. Heard, J.S. Preston, D.J. Parsons, J. Cox, G.C. Allen, Visualisation of the distribution of ink components in printed coated paper using focused ion beam techniques, Colloids Surf. A Physicochem. Eng. Asp. vol. 244 (1–3) (2004) 67–71, https://doi.org/10.1016/J.COLSURFA.2004.05.012.

[13] R.C. Daniel, J.C. Berg, Spreading on and penetration into thin, permeable print media: Application to ink-jet printing (no. SPEC. ISS), Adv. Colloid Interface Sci. vol. 123–126 (2006) 439–469, https://doi.org/10.1016/J.CIS.2006.05.012.

[14] K. Bülow, et al., The penetration depth and lateral distribution of pigment related to the pigment grain size and the calendering of paper, Nucl. Instrum. Methods Phys. Res. Sect. B Beam Interact. Mater. At. vol. 189 (1–4) (2002) 308–314, https://doi.org/10.1016/S0168-583X(01)01076-X.

[15] D.M. Desjumaux, D.W. Bousfield, T.P. Glatter, R.L. Van Gilder, Influence of latex type and concentration on ink gloss dynamics, Prog. Org. Coat. vol. 38 (2) (2000) 89–95, https://doi.org/10.1016/S0300-9440(00)00078-3.

[16] R. Li, Y. Zhang, Y. Cao, Z. Liu, Ink Penetration of Uncoated Inkjet Paper and Impact on Printing Quality, BioResources vol. 10 (4) (2015) 8135–8147, https://doi.org/10.15376/BIORES.10.4.8135-8147.

[17] C.H. Koo, A.W. Mohammad, F. Suja, Effect of cross-flow velocity on membrane filtration performance in relation to membrane properties, N. pub Balaban vol. 55 (3) (2014) 678–692, https://doi.org/10.1080/19443994.2014.953594.

[18] K.J. Howe, M.M. Clark, Effect of coagulation pretreatment on membrane filtration performance, J. / Am. Water Work. Assoc. vol. 98 (4) (2006), https://doi.org/10.1002/J.1551-8833.2006.TB07641.X.

[19] G. Boccardo, et al., A review of transport of nanoparticles in porous media: From pore- to macroscale using computational methods, Nanomater. Detect. Remov. Wastewater Pollut. (2020) 351–381, https://doi.org/10.1016/B978-0-12-818489-9.00013-X.

[20] A. Elrahmani, R.I. Al-Raoush, H. Abugazia, T. Seers, Pore-scale simulation of fine particles migration in porous media using coupled CFD-DEM, Powder Technol. vol. 398 (2022), 117130, https://doi.org/10.1016/J.POWTEC.2022.117130.

[21] Y. Zhou, L. Chen, Y. Gong, S. Wang, Pore-scale simulations of particles migration and deposition in porous media using LBM-DEM coupling method, *2021, Vol. 9, Page 465*, vol. 9, Process (3) (2021) 465, https://doi.org/10.3390/PR9030465.

[22] C.J. Kuijpers, H.P. Huinink, N. Tomozeiu, S.J.F. Erich, O.C.G. Adan, Sorption of water-glycerol mixtures in porous Al2O3 studied with NMR imaging, Chem. Eng. Sci. vol. 173 (2017) 218–229, https://doi.org/10.1016/j.ces.2017.07.035.

[23] N. Riefler, M. Ulrich, M. Morshäuser, U. Fritsching, Particle penetration in fiber filters, Particuology vol. 40 (2018) 70–79, https://doi.org/10.1016/J.PARTIC.2017.11.008.

[24] Y. Li and B. He, Characterization of ink pigment penetration and distribution related to surface topography of paper using confocal laser scanning microscopy, *BioResources*, vol. 6, no. 3, pp. 2690–2702.

[25] C. Waldner, U. Hirn, Ultrasonic liquid penetration measurement in thin sheets—physical mechanisms and interpretation, *2020, Vol. 13, Page 2754*, vol. 13, Mater (12) (2020) 2754, https://doi.org/10.3390/MA13122754.

[26] C. Waldner, A. Mayrhofer, U. Hirn, Measuring liquid penetration in thin, porous sheets with ultrasound and drop absorption – scope and limitations, Colloids Surf. A Physicochem. Eng. Asp. vol. 650 (2022), 129551, https://doi.org/10.1016/J.COLSURFA.2022.129551.

[27] C.J. Kuijpers, T.A.P. van Stiphout, H.P. Huinink, N. Tomozeiu, S.J.F. Erich, O.C.G. Adan, Quantitative measurements of capillary absorption in thin porous media by the Automatic Scanning Absorptometer, Chem. Eng. Sci. vol. 178 (2018) 70–81, https://doi.org/10.1016/j.ces.2017.12.024.

[28] R. Nicasy, H.P. Huinink, S.J.F. Erich, O.C.G. Adan, High-speed NMR imaging of capillary action in thin nontransparent porous media, Phys. Rev. E vol. 104 (4) (2021), L043101, https://doi.org/10.1103/PhysRevE.104.L043101.

[29] R.J.K. Nicasy, H.P. Huinink, S.J.F. Erich, O.C.G. Adan, N. Tomozeiu, Ultra Fast Imaging NMR method for measuring fast transport processes in thin porous media, Magn. Reson. Imaging vol. 103 (2023) 61–74, https://doi.org/10.1016/j.mri.2023.06.009.

[30] R.J.K. Nicasy, et al., Liquid uptake in porous cellulose sheets studied with UFI-NMR: Penetration, swelling and air displacement, Carbohydr. Polym. 326 (2024) 121615, https://doi.org/10.1016/J.CARBPOL.2023.121615.

[31] T. Baumann, C.J. Werth, Visualization of colloid transport through heterogeneous porous media using magnetic resonance imaging, Physicochem. Eng. Asp. vol. 265 (2005) 2–10, https://doi.org/10.1016/j.colsurfa.2004.11.052.

[32] C.J. Kuijpers, H.P. Huinink, N. Tomozeiu, S.J.F. Erich, O.C.G. Adan, Nano-particle dynamics during capillary suction, J. Colloid Interface Sci. 521 (2018) 69–80., https://doi.org/10.1016/J.JCIS.2018.03.023.

[33] S. Lu, J. Forcada, Preparation and characterization of magnetic polymeric composite particles by miniemulsion polymerization, J. Polym. Sci. Part A Polym. Chem. vol. 44 (13) (2006) 4187–4203, https://doi.org/10.1002/POLA.21525.

[34] A. Merbach, L. Helm, and É. Toth, The Chemistry of Contrast Agents in Medical Magnetic Resonance Imaging: Second Edition, *The Chemistry of Contrast Agents in Medical Magnetic Resonance Imaging: Second Edition*, Feb. 18, 2013.

[35] myHealthbox, Clariscan 0,5 mmol/ml Oplossing voor | myHealthbox, 2022. ⟨https://myhealthbox.eu/nl/clariscan-05-mmol-ml-oplossing-voor-injectie/5135676⟩ (accessed Mar. 08, 2022).

[36] J.L. Markley, W.J. Horsley, M.P. Klein, Spin-lattice relaxation measurements in slowly relaxing complex spectra, J. Chem. Phys. vol. 55 (7) (. 2003) 3604, https://doi.org/10.1063/1.1676626.

[37] R. Nicasy, H. Huinink, B. Erich, and O. Adan, NMR Profiling of Reaction and Transport in Thin Layers: A Review, *Polym. 2022, Vol. 14, Page 798*, vol. 14, no. 4, p. 798, Feb. 2022, ⟨doi:10.3390/POLYM14040798⟩.

[38] E.D. Ostroff, J.S. Waugh, Multiple spin echoes and spin locking in solids, Phys. Rev. Lett. vol. 16 (24) (1966) 1097–1098, https://doi.org/10.1103/PhysRevLett.16.1097.

[39] Y. Zhang, J. Cheng, and W. Liu, Characterization and Relaxation Properties of a Series of Monodispersed Magnetic Nanoparticles, 2019, ⟨doi:10.3390/s19153396⟩.

[40] Y. Gossuin, et al., Characterization of commercial iron oxide clusters with high transverse relaxivity, J. Magn. Reson. Open vol. 10–11 (2022), 100054, https://doi.org/10.1016/J.JMRO.2022.100054.